**RESEARCH ARTICLE**

# Machine Learning Approach in Optimal Localization of Tumor Using a Novel SIW-Based Antenna for Improvement of Ablation Zone in Hepatocellular Carcinoma

**SUYASH KUMAR SINGH** AND **AMAR NATH YADAV**

Department of Electronics and Communication Engineering, Indian Institute of Information Technology at Allahabad, Allahabad 211015, India

Corresponding author: Suyash Kumar Singh (rse2019004@iiita.ac.in)

**ABSTRACT** In recent years, hepatocellular carcinoma has been the leading cause of cancer-related mortality and thermal ablation procedures such as MWA (microwave ablation) and RFA (Radiofrequency ablation) provide a viable alternative to radiation and surgical excision. Due to uneven ablation and tissue charring in RFA, MWA offers faster and uniform heating as a result of its higher operating frequency. In MWA, the antenna probe heats the tissue to the point of cell necrosis using electromagnetic heating. In this aspect, a substrate-integrated waveguide (SIW) antenna is designed to work at 2.45 GHz. Further, a finite element method (FEM) is employed to model the probe and the liver tissue environment. Within 10 minutes of application time, a maximum ablation diameter of 32 mm (transversal-T) and 25 mm (axial-A) is achieved at 20W of power. Since the position of the applicator probe is of utmost importance, the relationship between the percentage of ablation, probe tip position, and tumor diameter is evaluated using ML- algorithm to estimate the ideal probe location for maximal tumor ablation and thus may improve clinical outcome.

**INDEX TERMS** Ablation zone, cat boost, microwave ablation antenna, support vector regression, XG boost.

## I. INTRODUCTION

Liver cancer is the third leading cause of cancer-related death and the fifth most common kind of cancer in the world with a terrible survival rate. Only 20% of patients are candidates for surgery and both primary and secondary hepatic tumor patients react poorly to chemotherapy and radiation therapy as a result of their harsh treatment protocol [1]

In such a situation, thermal ablation procedures are a viable option compared to surgical resection due to their advantages which include minimum invasiveness, shorter hospital stays, faster return to normal activities, and lower healthcare expenses [2].

Microwave ablation (MWA) is a relatively new and well-approved clinical ablation method among the current thermal ablation treatments. The primary objective of MWA is to cause necrosis in cancer cells by increasing the temperature between 50-100 °C. The thermal damage may be restricted to the cancerous tissue with a suitable margin of safety to minimize the chance of damage to healthy tissue. Researchers anticipate that the microwave ablation applicator should produce a spherical ablation zone due to the almost spherical form of most tumors [3]. Therefore, an important feature of therapeutic microwave ablation antennas is to create a spherical ablation zone for tumor ablation, and hence, several types of microwave ablation antennas have been introduced to date. In previous studies, coaxial cable based MWA antennas such as a monopole, co-axial choke, co-axial slot, and coaxial helical antennas were investigated [4]. Since currents flow through both the inner and outer conductor of the coaxial cable due to the unbalanced monopole antenna construction, as a result, the ablation zone is extended along the coaxial line and healthy tissue along the antenna insertion route may be burnt which should be avoided in practical applications [5].

A choke operating as a balun is introduced to lessen the unwanted current distribution at the outer conductor of the co-axial cable. By introducing such a choke as an open circuit at an appropriate place on the outer conductor of a coaxial line, it is feasible to generate a high impedance and prevent the flow of current in the outer conductor. However, the additional balun design may increase the cross-section area of the antenna making it unsuitable for minimally invasive therapy [6]. Further to overcome such a shortcoming, a coaxial slot antenna is introduced with a balun-free structure but its performance is hampered by the surrounding medium since the slot of the outer conductor makes direct contact with tissue. Another kind of antenna without a balun is the coaxial helical antenna. A helical construction is often included in a coaxial line to provide maximum voltage and minimum current at a certain point along the feeding line. The effective high impedance acts as a natural choke at this location, dampening the current flowing in the outer conductor of the feeding coaxial cable and providing a confined ablation zone. However, this structure is difficult and expensive to construct and it is especially challenging to create a matching network within the coaxial cable [7].

The novelty of this work is to design an axis-symmetric cross-like antenna that resembles a normal mode helical antenna integrated on a substrate-integrated coaxial cable (SICL) and can create a highly localized circular ablation zone as contrary to the antenna demonstrated in [8], without using the extended balun structure. The main advantage of SIW based structure is that it provide better power handling capacity as compared to microstrip structure and hence can be useful in high power application such microwave ablation. Also, SIW can also be fabricated with low cost mass production using plated though hole (PTH) technology. The designed antenna is fed with a GCPW (grounded coplanar waveguide) feed connected to an impedance transformation structure along with an inset transition connected to SICL which is further connected to an appropriate antenna location which restrain the need for a matching network in the antenna applicator. Furthermore, the specific absorption rate (SAR) of the applicator is also analyzed using temperature-dependent electrical and thermal properties. Also, for efficient ablation and optimal localization of the novel antenna applicator various machine learning algorithms were incorporated in this study as ML algorithms were found to be useful in medical diagnostics and treatment protocols [9].

## II. DESIGN METHODS OF THE ANTENNA APPLICATOR

The SIW structure consists of a dielectric substrate covered by metallic plate on both sides. The two parallel rows of via-metallic holes connecting the upper and lower conductors act as wall of the waveguide to prevent leakage of electromagnetic fields. The distance between the two parallel sets of vias and center to center distance between each via can be optimized for better propagation of the wave. The antenna structure consists of cross-like microstrip lines on the upper and lower part of the substrate at the distal end
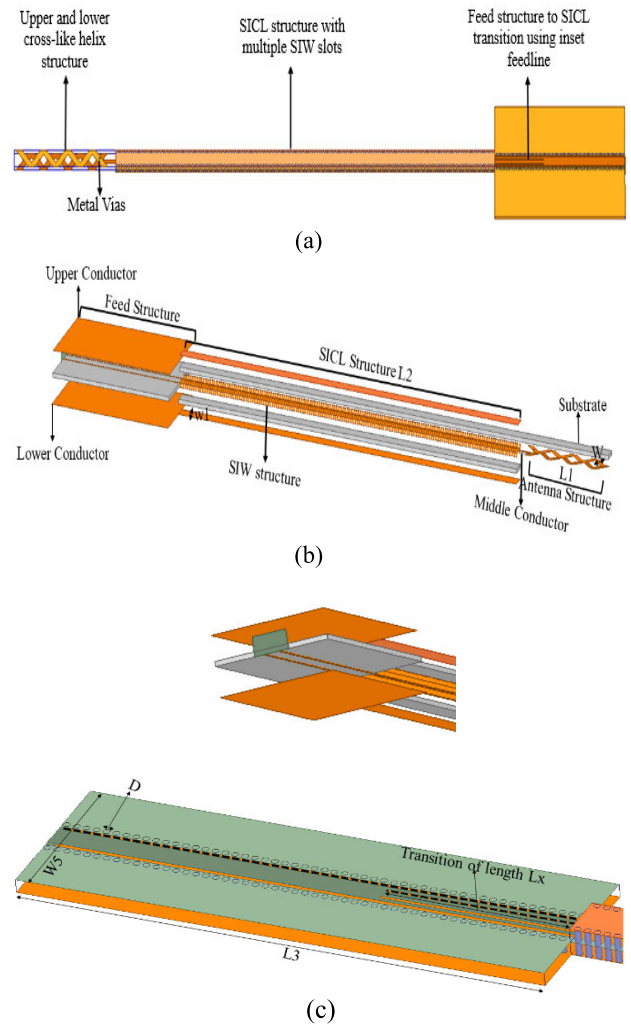


(a)



(b)



(c)

**FIGURE 1.** (a) Top view of the antenna applicator 1 (b) Explosive view of the antenna 1 (c) Impedance transformation structure of the antenna.

and are shorted using the metal via as shown in Figure 1(a). Further, the antenna and the SICL structure are connected using the middle conductor as shown in Figure 1(b) which is further connected to a feeding structure. According to the difference in the functionality of each structure, the whole setup is divided into the antenna structure part, SICL waveguiding part, and an SIW impedance matching part.

### A. ANTENNA DESIGN

At the distal tip of the applicator, a radiating intertwined helix structure with a cross-like pattern is connected to SICL feedline, as shown in Figures 1(a) and 1(b). To provide a symmetrical ablation pattern, a cross-like helix structure is mounted on the upper and lower side of the substrate which can provide a spherical ablation zone. The dimension of the antenna is shown in Table 1 considering PCB fabrication capability. The extended middle conductor is used to tap the helix structure to achieve impedance matching to the 50-ohm line as shown in Figure 1(b). Further, since the impedance is very low at the feed point of the antenna, therefore the periodic cross-like

**TABLE 1.** Dimension of the applicator.

| Antenna Structure | Symbol | Value |
|---|---|---|
| Width of the cross-like structure | w | 1.5 mm |
| Length of cross-like structure | $L_1$ | 22.5 mm |
| No. of turns in a cross-like pattern | N | 3 |
| **Guiding Structure (SICL)** | | |
| Width of upper/lower Conductor of SICL | $w_1$ | 2.75 mm |
| Width of the middle Conductor of SICL | $w_2$ | 0.5 mm |
| Slot Diameter | D | 0.4 mm |
| Length of upper/ lower conductor | $L_2$ | 92.5 mm |
| Slot spacing | $L_4$ | 0.2 mm |
| **Impedance transformation structure** | | |
| Width of upper/lower conductor | $w_5$ | 16 mm |
| Length of conductor | $L_3$ | 32 mm |

structure is added to improve the impedance matching with the feed line.

### B. WAVE-GUIDING STRUCTURE

The main wave-guiding portion of the antenna is based on a SICL. Figure 1(b) depicts an explosive view of the antenna applicator. Two dielectric layers and three metal layers with a thickness of 0.035 mm are used to create a conventional SICL-based structure for the guiding component. As per Figure 1(b), the three metal layers are interconnected by slots with a diameter of D. If the diameter D of the slot is less than $\frac{\lambda}{10}$ and if the distance $L_4$ between adjacent vias is less than twice the diameter D then the two rows of vias may be regarded as two metal walls [10]. As the thickness of two SICL dielectric layers is of height $h = 0.5$ mm, an affordable low-loss dielectric RT Duroid 5870 is employed. At roughly 2.45 GHz, the relative dielectric constant and loss tangent of the dielectric are 2.33 and 0.001, respectively; thus, the SICL can be considered aa a lossless transmission line. The equation for characteristic impedance is obtained by using a 50-ohm impedance for the SICL and is given by:-

$$Z_p = \frac{1}{V_p C_{unit}} \qquad (1)$$

where, $V_p$ is the phase velocity of the wave inside the SICL and $C_{unit}$ is the per unit length capacitance of the SICL. The middle conducting layer acts as an inner conductor of the waveguide whose thickness is negligible. Hence, the
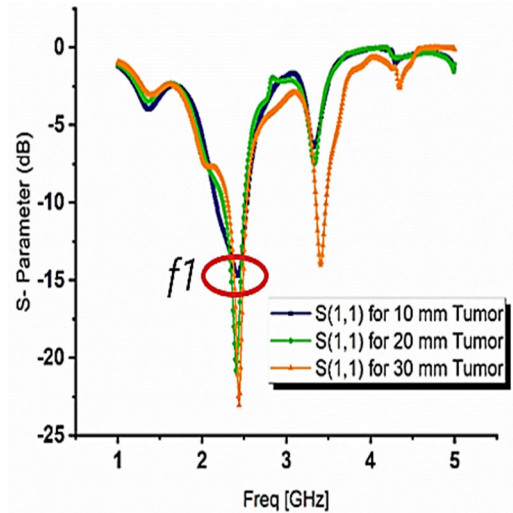


**FIGURE 2.** Reflection coefficient of the antenna obtained in tumor domain of diameter 10 mm, 20 mm and 30 mm.

capacitance $C_{unit}$ for the SICL can be calculated by [10] :-

$$C_{unit} = 2\epsilon \left( \frac{w_2}{h} \right)$$
$$+ \frac{4\epsilon}{\pi} \left[ ln \left( \frac{w2^2 + h^2}{4h^2} \right) + \frac{2h}{w_2} arctan \left( \frac{2w_2}{h} \right) \right]$$
$$+ \frac{4\epsilon}{\pi} \left[ ln \left( \frac{w2^2 + h^2}{4w_2^2} \right) + \frac{2w_2}{h} arctan \left( \frac{h}{w_5} \right) \right] \qquad (2)$$

### C. IMPEDANCE TRANSFORMATION STRUCTURE

An impedance transformation structure is employed to keep the ablation zone confined at frequency $f_1$ while addressing the impedance mismatching issue, as illustrated in Figure 1(c). Initially, at the start of the SICL-based applicator, GCPW (grounded coplanar waveguide) is implemented which is further connected to the SICL using the inset technique. Similar to the SICL, two rows of vias link the ground planes. For impedance matching, the dimensions mentioned in Table 1 are meticulously designed. Since the highest current is in the center of the GCPW impedance transformation structure, the distance $L_x$ is changed to optimize the 50-ohm input impedance to match the GCPW- SICL interface and SICL- helix interface. Further, the reflection coefficient of the antenna in the simulated tissue environment with varying tumor size is shown in Figure 2. A reflection coefficient of -24 dB is observed in tumor with 30 mm of diameter and hence can be advantageous in the efficient delivery of microwave power to the tissue with minimal loss of power.

### III. THERMAL AND ELECTRICAL TISSUE PROPERTIES

As tissue is formed of veins and arteries with sizes as small as a few microns, introducing thermal boundary condition would complicate the assessment of the bio-heat transfer model without influencing the results of clinical outcomes. Therefore, blood vessels are assumed to be missing from
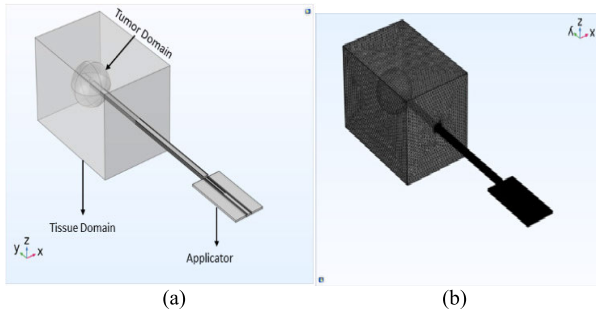
**FIGURE 3.** (a) Antenna applicator in simulated tissue environment (b) Element size-dependent meshing with maximum meshing in complex applicator domain.
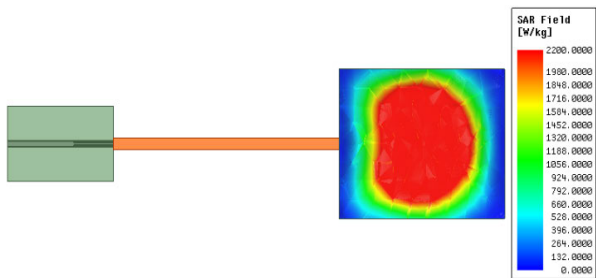


**FIGURE 4.** Near Spherical SAR Pattern of the proposed antenna.

the investigated tissue but their influence is included by considering all thermo-physical components into the conduction equation known as Penne's Bio-Bioheat model for restricted space and is given by [11]:-

$$\rho C_p \frac{dT}{dt} - \nabla . (k\nabla T) = \rho_b C_{p,b} \omega_b (T_b - T) + Q_{met} + Q_e$$

(3)

where, $Q_{met}$[W/m$^2$] is the metabolic heat of the tissue, $\rho$ is the density of tissue [kg/m$^3$], $C_p$ is the tissue-specific heat capacity [J/kg-K], T temperature of the tissue [K], $k$ is the tissue thermal [W/m-K], $\omega_b$ rate of blood perfusion [1/s], $\rho_b$ density of blood [kg/m$^3$], $C_{p,b}$ blood specific heat [j/kg-K], and $T_b$ is the arterial temperature of blood [K].

The energy balance law over a conserved volume as given in equation (3) is defined by the total energy gained by the tissue which is equal to conductive heat generated within the tissue followed by convective heating due to blood perfusion effect, the heat generated due to metabolic process and external heat applied to the tissue during microwave ablation, respectively.

A 3D finite element technique (FEM) using Comsol Multiphysics 5.5 software is employed in this work to solve a coupled electromagnetic field and heat transfer model. The model consists of an antenna applicator, tissue domain and tumor domain as shown in Figure 3(a). The meshing is varied according to the complexity of the structure with finer meshing for the antenna applicator (with element size of 0.0001 mm) and normal to coarse meshing (with element size of ranging from 0.001mm to 0.01mm) for tumor and tissue

**TABLE 2.** Temperature-dependent electrical properties.

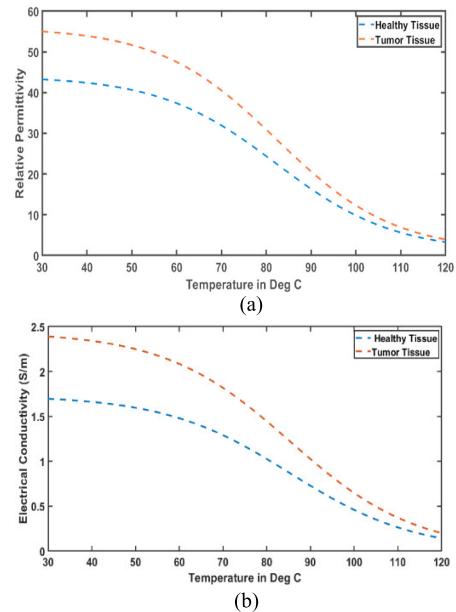| Electrical properties | $a_1$ | $a_1$ | $a_1$ | $R^2$ |
|---|---|---|---|---|
| $\varepsilon_r$ | 0.0764 | 82.271 | 48.391 | 0.8570 |
| $\sigma$ | 0.0697 | 85.375 | 2.173 | 0.7881 |



**FIGURE 5.** (a) Plot of relative permittivity with temperature in healthy and tumorous tissue (b) Plot of electrical conductivity with temperature in healthy and tumorous tissue.

domain. The total number of tetrahedral mesh elements are 663581, as shown in Figure 3(b).

Further, the tissue boundary condition is resolved using the classical Helmholtz wave equation and is given by [12]:

$$\nabla^2 \vec{E} - \beta_0^2 \left( \varepsilon_r - \frac{j\sigma}{w\varepsilon_0} \right) . \vec{E} = 0$$

(4)

where E is the electric field complex time-harmonic vector [V/m], $\beta_0$ is the wave-wave number space [m$^{-1}$] $\varepsilon_r$ is relative permittivity, $\sigma$ is electric conductivity [S/m], $\omega$ is angular frequency [rad/s] and $\varepsilon_0$ is the permittivity of free space [F/m].

Figure 4 shows the SAR distribution of the applicator in the Ansys HFSS 18 software considering the permittivity at 50. Since the applicator is aimed to be inserted into the tumor tissue therefore, a permittivity value of 50 is chosen to match with the actual permittivity value of the tumor (i.e., permittivity of $50 \pm 2$) at 60 °C, as shown in figure 5(a), [13]. Further, it can also be conferred that due to the matching of the antenna, the elongated SAR pattern along the axis of the antenna is minimized. However, the above analysis is considered without including the tissue environment.

**TABLE 3.** Tissue thermo-electrical properties.

| Liver Thermal Properties | Thermal Conductivity [W/m/K] | Heat capacity [J/(kg·K)] | Frequency factor [1/s] | Activation energy [J/mol] |
|---|---|---|---|---|
| | 0.52 | 3540 | $7.39 \times 10^{3}$ $9$ | $2.577 \times 10$ $5$ |
| Blood Thermal properties | Blood perfusion rate [1/s] | Blood Density [kg/m$^3$] | Specific heat Capacity [J/(kg·K)] | Temperature [°C] |
| | 0.00361 | 1000 | 3639 | 37 |
| Tissue Electrical Properties | Relative permeability | Electrical conductivit-y [S/m] | Resistivity [Ω.m] | Relative Permittivity |
| | 1 | Figure 5 (b) | 0.59 | Figure 5(a) |



**FIGURE 6.** Degree of tissue injury with respect to time (t = 0,1,4,6,8,10 min) with a value of 1 indicates 100 percent ablation.

Therefore, for further analysis, COMSOL Multiphysics software is incorporated in this study.

Furthermore, MWA generates structural anomalies in the tissue as a consequence of the elevated temperatures generated during tissue heating and cell necrosis near the antenna resulting in alterations to the dielectric and thermal properties of the tissue and as a result, the electromagnetic power distribution is severely affected. Such modifications are not accounted for in either ex-vivo setups or FEM simulations, leading to overestimated ablation zones. To correct this anomaly, temperature-dependent permittivity and electrical conductivity by using the sigmoidal curve-fitting approach is incorporated in this study. The fitted curve equation for permittivity and conductivity in healthy and malignant liver tissue is provided by [13]:-

$$\varepsilon_r (T) = a_3 \left[ 1 - \frac{1}{1 + e^{a_1 (a_2 - T)}} \right] + 1 \qquad (5)$$

$$\sigma (T) = a_3 \left[ 1 - \frac{1}{1 + e^{a_1 (a_2 - T)}} \right] \qquad (6)$$

where, the values of each regression constant and the root mean square of the regression are given in Table 2. The temperature-dependent sigmoidal model of (a) relative permittivity and (b) electric conductivity for normal and malignant tissues is shown in Figure 5. As predicted, the relative permittivity and conductivity of liver tumors are around 20% and 25% greater, respectively, than those of normal liver tissue. During microwave ablation, the water content in the tissue evaporates and the ionic property of the tissue decreases as t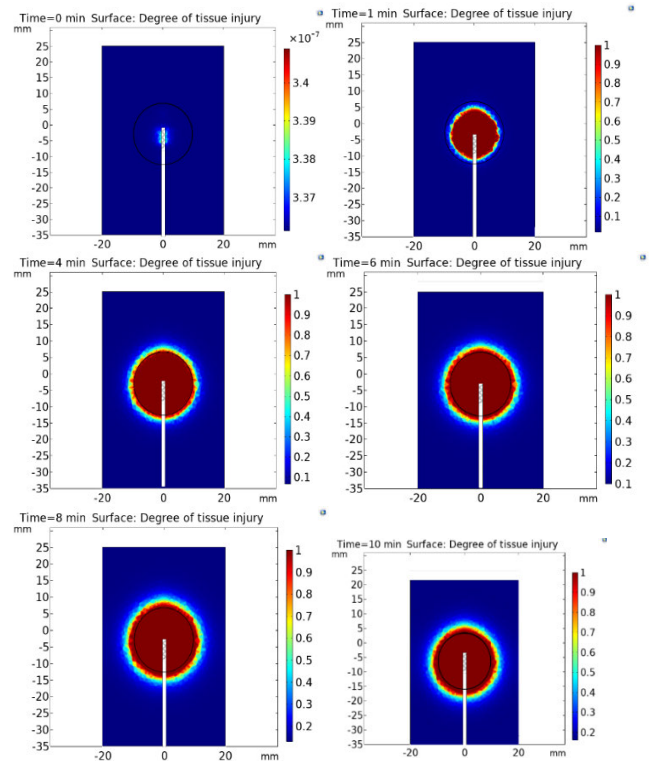he temperature rises leading to a change in the conductivity and permittivity of the medium. Furthermore, the slope of dielectric characteristics and electrical conductivity with temperature is similar in both healthy and cancerous tissues.

The temperature-dependent conductivity and permittivity are further incorporated in 3-D model of liver tissue with 20 mm tumor. The tissue and tumor thermo-electrical parameters are shown in Table 3.

In addition, using the Arrhenius equation, the simulated model calculate the rate of tissue damage ($\alpha$) given by [14].

$$\frac{\partial \alpha}{\partial t} = (1 - \alpha)^n * A e^{\frac{-\Delta E}{RT}} \qquad (7)$$

where, A is the frequency factor in [1/s], $\Delta$ E is the activation energy for tissue necrosis in (j/mol), R is the Gas constant, and T is the temperature. The proportion of tissue damage caused by microwave ablation is calculated using:-

$$\theta_d = 1 - e^{-\alpha} \qquad (8)$$

When the temperature is more than the tissue damage temperature $T_d$ for more than time-period $t_d$, the rate of damage is given by:-

$$\alpha = \frac{1}{t_d} \int_0^t \varphi_{d,h} dt \qquad (9)$$

where,

$$\varphi_{d,h}(t) = \begin{cases} 1 & if \ T > T_{d,h} \\ 0 & otherwise \end{cases} \qquad (10)$$
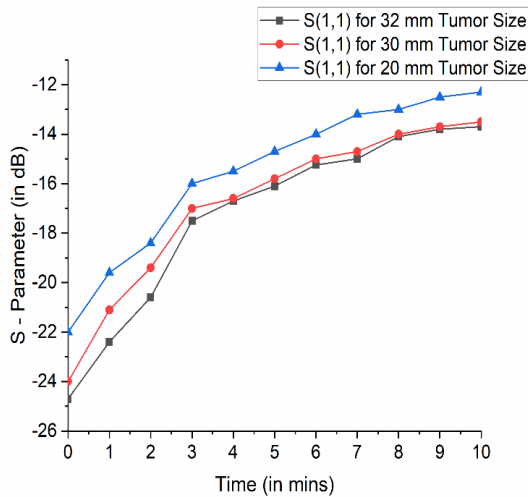
**FIGURE 7.** Reflection coefficient plot with respect to time (0:1:10) minutes.

$\varphi_{d,h}(t)$ is the ratio of period of application time T to time limit of necrosis $T_{d,h}$. When the ratio reaches the value 1, it means the tissue has reached necrosis. The fraction of tissue necrotic is a quantity with min $(\alpha, 1)$ value. As depicted in Figure 6, ablation starts along the normal direction of the antenna applicator with maximum ablation or tissue necrotic reached at the time (t) equal to 10 minutes. The antenna applicator successfully ablated the tumor tissue of size 20 mm. Also, since the antenna applicator is in matched condition, a spherical ablation zone is reached with minimal elongation along the axial direction of the antenna and hence, reduces the chance of ablating healthy tissue along the applicator length.

Further, the Figure 7 shows the reflection coefficient with respect to time for three different tumor sizes. The value of $S_{11}$ is calculated for the time interval of 0-10 minutes. Since deviation in permittivity and conductivity is faster due to increase in temperature (as shown in Figure 5), therefore, a sharp change is observed in $S_{11}$. However, at higher temperature (i.e., above 100 °C) the value of permittivity and conductivity saturates and hence the value of $S_{11}$ also move towards saturation The effect can also be explained from evaporation of water content above 100°C resulting in saturated permittivity and electrical conductivity of the tissue domain.

Further, the maximum value of $S_{11}$ attained ie below 10 dB range which shows that more than 90 percent of the applied power is transmitted to the tissue and the applicator remain in matched condition thoughout the application time. Further, since the permittivity of the tumor depends upon the level of malignancy, Figure 8 shows the specific absorption rate for permittivity value of 25, 35 and, 55. As can be seen that the SAR value reduces with an increase in permittivity along the length of the applicator. Few of the SAR evaluation points from 0-30 mm is shown in the figure 8(a) at a distance of 2 mm from the applicator.
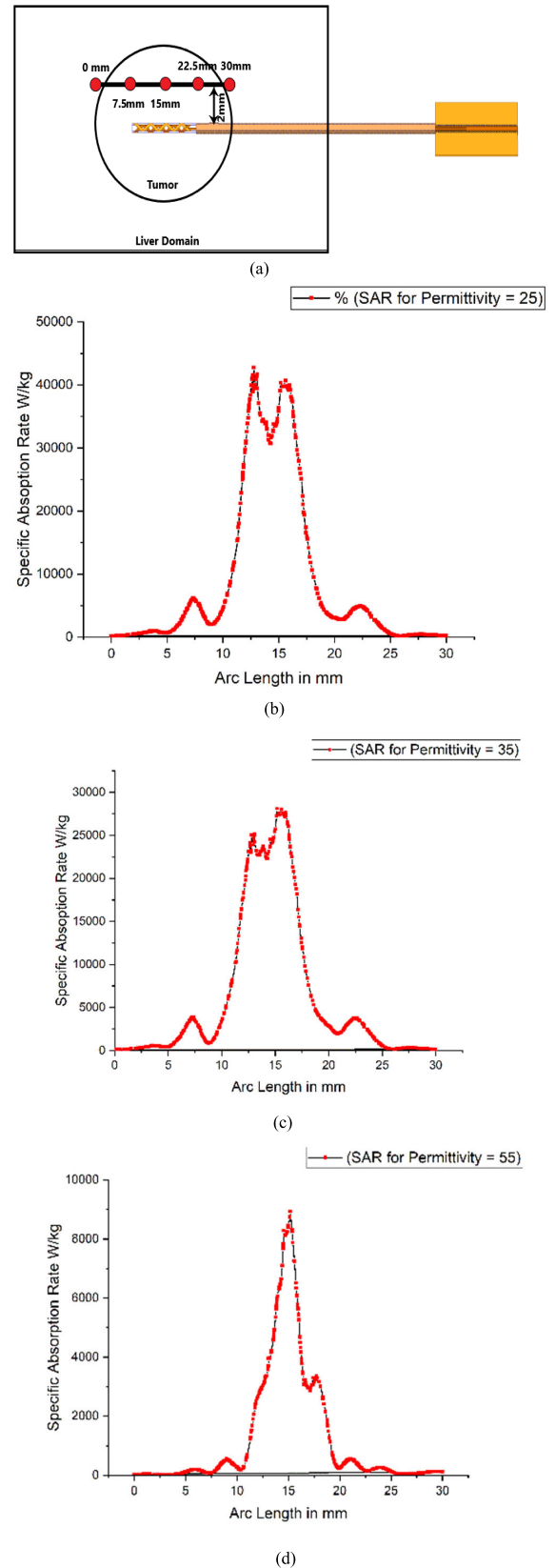








**FIGURE 8.** (a) Data points for evaluation of SAR pattern (b), (c) and (d) SAR along the arc length of the antenna application with permittivity values of 25, 35 and 55 respectively.
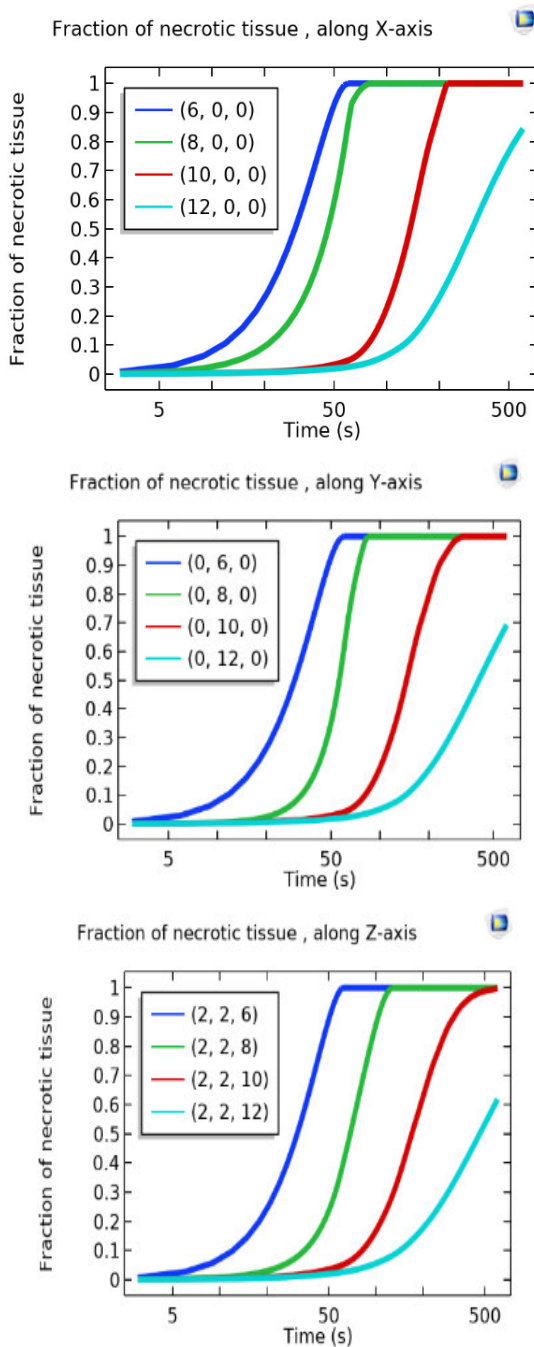
**FIGURE 9.** Rate of ablation along axial (z) and transversal direction (x and y) along the antenna applicator.



**FIGURE 10.** (a) Calculated and predicted ablation percentage using simple regression (b) Residuals plot with maximum error in ablation percentage prediction of 13 percent.

The reduction in SAR is due to the impedance mismatch of the antenna as the surrounding permittivity increases. However, at a permittivity of 55, the SAR value is still in the satisfactory range but such cases need to be evaluated while designing an ablation antenna in order to improve and match clinical outcomes with simulated results. Further, Figure 9 shows the rate of necrotic tissue along the axial (z) and transversal direction (x and y) of the applicator. This shows that the ablation zone is similar in all the directions, depicting
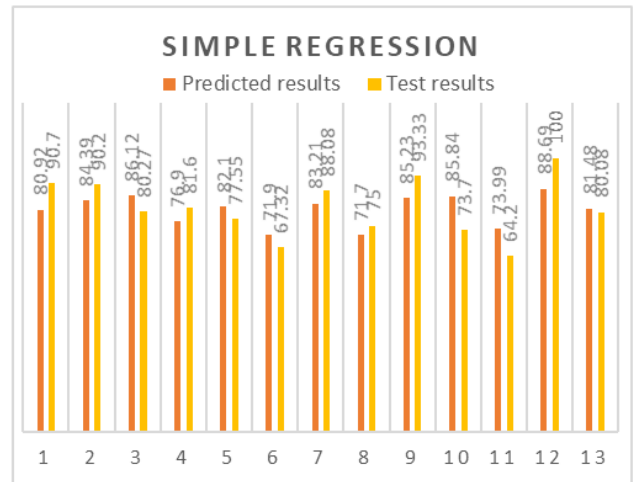
a near-spherical ablation zone. Since the heat generated by the applicator is higher near the antenna, therefore, faster rate of tissue necrosis is observed in the proximity of the applicator.

Further, the optimal positioning of the applicator inside the tumor is of utmost important to ablate the tumor properly as misplaced location not only destroys the nearby healthy tissue but also fraction of the tumor may go untreated and hence may cause recurrence of the HCC. Therefore, optimal localization of tumor is necessary to improve the clinical outcome. In this regard, various machine learning algorithm were exploited to establish a relationship between tumor size, tumor location and ablation percentage. Such a relationship is also helpful in optimum use of power for variable size of tumor since the ablation percentage is dependent on applied power.

## IV. MACHINE LEARNING ALGORITHM METHODOLOGY

To predict the dependent response 'y' (ablation percentage) using the tumor location (distance of the center of tumor to the tip of applicator) and tumor diameter as an independent

**TABLE 4.** Tumor size and location vs ablation percentage.

| Tumor Size | Tumor Location | Ablation Percentage | Tumor Size | Tumor Location | Ablation Percentage |
|---|---|---|---|---|---|
| 24 | -8 | 68.88 | 26 | -4 | 80.08 |
| 24 | -6 | 76.55 | 26 | -2 | 88.08 |
| 24 | -4 | 84.44 | 26 | 0 | 100 |
| 24 | -2 | 93.33 | 26 | 2 | 100 |
| 24 | 0 | 100 | 26 | 4 | 95.91 |
| 24 | 2 | 100 | 26 | 6 | 87.77 |
| 24 | 4 | 100 | 26 | 8 | 79.55 |
| 24 | 6 | 88.89 | 28 | -8 | 57.66 |
| 24 | 8 | 82.22 | 28 | -6 | 64.44 |
| 26 | -8 | 66.6 | 28 | -4 | 71.11 |
| 26 | -6 | 72 | 28 | -2 | 76.27 |
| 28 | 0 | 93.28 | 32 | 6 | 80.43 |
| 28 | 2 | 99.72 | 32 | 8 | 73.7 |
| 28 | 4 | 93.22 | 34 | -8 | 67.32 |
| 28 | 6 | 84.77 | 34 | -6 | 75 |
| 28 | 8 | 76.27 | 34 | -4 | 80.76 |
| 30 | -8 | 64.2 | 34 | -2 | 86.53 |
| 30 | -6 | 72.22 | 34 | 0 | 81.6 |
| 30 | -4 | 76.6 | 34 | 2 | 83.6 |
| 30 | -2 | 82.209 | 34 | 4 | 81.45 |
| 30 | 0 | 90.7 | 34 | 6 | 77.55 |
| 30 | 2 | 97.7 | 34 | 8 | 71.42 |
| 30 | 4 | 90.2 | 36 | -8 | 60.87 |
| 30 | 6 | 80.27 | 36 | -6 | 66.66 |
| 30 | 8 | 76.89 | 36 | -4 | 71.66 |
| 32 | -8 | 67.32 | 36 | -2 | 76.6 |
| 32 | -6 | 75 | 36 | 0 | 75.08 |
| 32 | -4 | 80.76 | 36 | 2 | 78.33 |
| 32 | -2 | 83.53 | 36 | 4 | 75.23 |
| 32 | 0 | 86.9 | 36 | 6 | 74.95 |
| 32 | 2 | 94.5 | 36 | 8 | 71.12 |
| 32 | 4 | 86.78 | | | |

variable 'x'( tumor location and tumor size), at first the simple linear regression (SR) is used.

Since the connection between the two variables is assumed to be linear, a linear function that properly predicts the response value or dependent variable (y) based on the feature of the independent variable (x) is required.

Here, the purpose is to choose a line that most closely fits the data in order to predict the response for any new feature values. This is referred to as the regression line. The regression line is represented by the following equation [15]: -

$$h(x_i) = \beta_0 + \beta_1 x_i \qquad (11)$$

where, $h(x_i)$ is the predicted response, $\beta_0$ and $\beta_1$ are the regression coefficient and are represented by the y-intercept and slope of a line.

Now, in order to evaluate the correctness of the model, least squares principle is used, which is denoted by: -

$$y_i = \beta_0 + \beta_1 x_i + \epsilon_i \qquad (12)$$

where, $y_i$ is the dependent variable or the ablation percentage obtained from the ablation datasets and $x_i$ is the independent variable (i.e centre of the tumor from the tip of antenna and size of tumor). The least square principle is used to determine the best fit regression line for the datasets and is also a convenient parameter to decide the efficacy of the algorithm. The total dataset (63 sample size) is divided into test sets (20%) and training sets (80%) for optimized performance. Further, to minimize the error function $\epsilon_i$, the cost function J is defined as: -

$$J(\beta_0, \beta_1) = \frac{1}{2n} \sum_{i=1}^{n} \epsilon_i^2 \qquad (13)$$
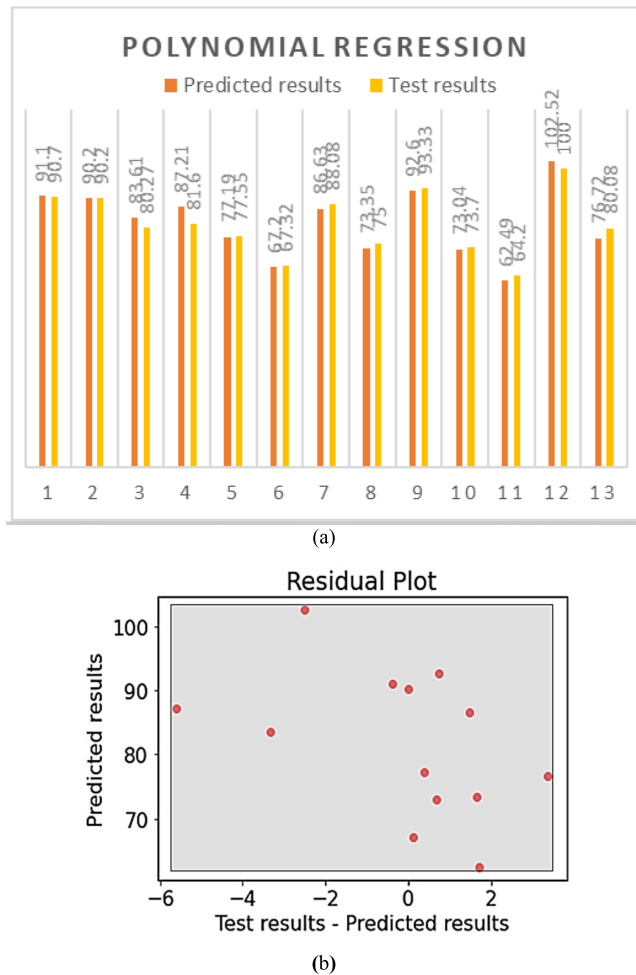
FIGURE 11. (a) Calculated and predicted ablation percentage using polynomial regression (b) Residuals plot with maximum error in ablation percentage prediction of 6 percent.

The task is to find the value of $\beta_0$, $\beta_1$ for which the value of $J(\beta_0, \beta_1)$ is minimum. Consequently, regression coefficients are defined as:-

$$\beta_1 = \frac{SS_{xy}}{SSxx} \quad \text{and} \quad \beta_0 = \bar{y} - \beta_1 \bar{x} \qquad (14)$$

where, $\bar{y}$ and $\bar{x}$ are the mean value of the sample, $SS_{xy}$ is the sum of cross-deviation of x and y and $SS_{xx}$ is the sum of deviation of x. The sample for tumor size and location is given in Table 4 along with the ablation percentage outcome. The ablation percentage is calculated as per the equation given in [6].

$$\text{Percentage of ablation} = \frac{\frac{4\pi}{3} \left(\frac{T}{2}\right)^2 \left(\frac{A}{2}\right) \text{ablation zone}}{\frac{4\pi}{3} \left(\frac{T}{2}\right)^2 \left(\frac{A}{2}\right) \text{tumor}} \times 100 \qquad (15)$$

In case of Simple Regression, as shown in Figure 10, the deviation observed in the test results and predicted result is from $-13$ percent to $+12$ percent which is significant and therefore, further algorithms were investigated.

### A. POLYNOMIAL REGRESSION

Polynomial regression is a specific example of multiple regression in which only one independent variable, $x_i$, is considered.

A model of polynomial regression with a single variable may be stated as:-

$$y_i = \beta_0 + \beta_1 x_i + \beta_2 x_i^2 + \beta_3 x_i^3 \ldots \ldots \ldots \beta_k x_i^k + \epsilon_i \quad (16)$$

where $i = 1,2,3,4,5\ldots$ N and k is the degree of the polynomial.

The R-squared(coefficient of determination) of the multiple regression is comparable to the simple regression, which is defined as follows:-

$$R^2 = 1 - \frac{SSE}{SST} = 1 - \frac{\sum_{i=1}^{n}(y_i - \hat{y}_i)^2}{\sum_{i=1}^{n}(y_i - \bar{y})^2} \qquad (17)$$

where SST represents the total sum of squares and $\bar{y}$ represents the arithmetic mean of the output variable, and $\hat{y}$ represents the predicted output. $R^2$ estimates the percentage of variance in the response variable (the percentage of ablation) and consequently, it is a crucial indicator of how well the regression model fits the data. $R^2$ always has a value between zero and one. An $R^2$ score of 0.9 or above is extremely excellent, while a value of 0.8 or higher is good. As illustrated in Figure 11, the observed divergence between the test set and the predicted result ranges from -6% to +4% with 80:20 training and test dataset ratio. Since residuals is used which measures the distance of regression line from the datapoints, RMSE (root mean square error) is included in this study which measures the standard deviation of the residuals.

Nevertheless, the degree of the polynomial equation is four resulting in a complicated interaction between the input and output variables. Also, such a regression algorithm may have overfitting issue and also lesser degree of freedom as compared to support vector regression (SVR).

### B. SUPPORT VECTOR REGRESSION

The main advantage of SVR is its excellent generalization and good prediction accuracy. The model built by support vector regression (SVR) is only dependent on a portion of the training data since the cost function used to construct the model disregards any training data that is near (within a threshold) to the model prediction [16].

Support vector machines (SVMs) are most often used in support vector regression (SVR). The essential idea behind SVM for regression and function estimation is the use of training data as $[(x_1, y_1 \ldots x_n, y_n)] \subset \aleph \times \xi$ where $\aleph$ signifies the space of input patterns, for instance $\xi^d$. The objective of support vector regression is to select f(x) that has the greater divergence from the real target $y_i$, for all of the training data while still being as flat as possible.

The function f(x) is defined by:

$$f(x) = <w, x> +b \text{ with } w \in \aleph, \qquad (18)$$

where $<..>$ denotes the dot product in $\aleph$. Flatness in the case of equation 17 requires a small w. One of the ways is to
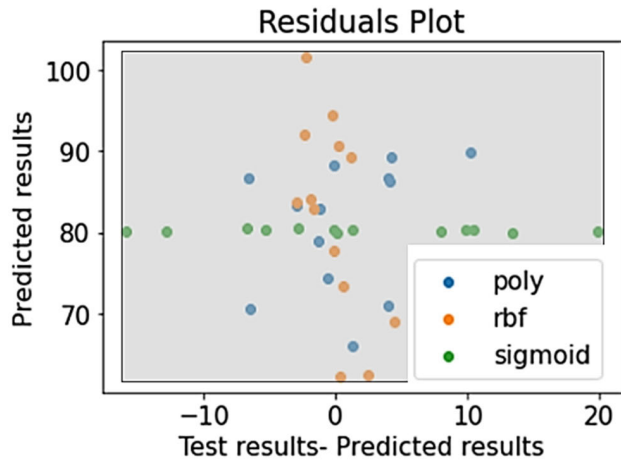
**FIGURE 12.** Residuals plot of ablation percentage for poly, rbf amd sigmoidal kernel of SVR with maximum prediction error observed in sigmoid kernel and minimum prediction error in rbf kernel.

minimize Euclidean norm i.e. $||w||^2$ which can be expressed as convex optimization problem.

$$\text{minimize } \frac{1}{2} ||w||^2 + C \sum_{i=1}^{n} (\vartheta_i + \vartheta_i^*)$$

$$\text{subject to } \begin{cases} y_i - <w, x_i> -b \leq \epsilon + \vartheta_i, \\ <w, x_i> +b - y_i \leq \epsilon + \vartheta_i^*, \\ \vartheta_i, \quad \vartheta_i^* \geq 0 \end{cases} \quad (19)$$

slack variables $\vartheta_i \vartheta_i^*$ are introduced to cope with otherwise infeasible constraints of the optimization problem. The regularization constant $C > 0$ sets the trade-off between the flatness of function $f$ and the tolerance for deviations greater than $\varepsilon$. A larger value of $C$ results in a smaller misprediction of the result, however, may result in overfitting of the predicted data. The $\varepsilon$-insensitive loss function $|\vartheta|\epsilon$ described by:-

$$\vartheta|\epsilon = \begin{cases} 0, & \text{if } |\vartheta| \leq \epsilon \\ |\vartheta| - \epsilon, & \text{otherwise} \end{cases} \quad (20)$$

In addition, regression problems have a nonlinear pattern (nonlinearity) and may be handled using kernel functions. Kernel is a non-linear version of regression that may be achieved by the so-called "kernel trick," in which a linear regression model is created in a high-dimensional feature space, $F(\varphi : X \rightarrow F)$ induced by a nonlinear kernel function specifying the inner product $K(x, x') = \varphi(x) \cdot \varphi(x')$ The kernel function, $K : \aleph \times \aleph \rightarrow \xi^d$ may be any "Mercer" kernel that is positive and definitive. The following are the three kernel functions used to predict the ablation percentage test:-

Polynomial kernel (poly) with degree d

$$K(x, x') = (x^T x' + 1)^d \quad (21)$$

Radial basis function (rbf) kernel with width $\sigma$

$$K(x, x') = e^{\left(-\frac{||x-x'||^2}{2\sigma^2}\right)} \quad (22)$$

Sigmoid with parameters $\kappa$ and $\theta$

$$K(x, x') = \tanh(\kappa x^T x' + \theta) \quad (23)$$

As seen in the Figure 12 the rbf kernel performs better than the polynomial and sigmoidal kernels. The residual margin of $-4$ to 6 ablation percent is observed in the case of rbf. Also, the predicted value of the sigmoidal kernel is out of bounds and may not be used in such a scenario. The predicted results of the poly kernel is also satisfactory but require 4th order of the polynomial. In conclusion, SVR with a rbf kernel performs better than polynomial regression and sigmoid kernel. However, the regularization constant ($C$) as shown in equation 18, in case of rbf and poly kernels are of the order of $10^3$ to minimize RMSE (root mean square error) and maximize $R^2$ which may eventually lead to overfitting. Such a problem of overfitting the datasets can be resolved through boosting algorithm with early stopping parameters.

### C. BOOST ALGORITHM
Gradient Boosting is a prominent technique for boosting. Since the above algorithms suffer from overfitting of data and complexity in formulization due to 4th order polynomial, therefore, gradient boosting is further incorporated in this study. Each predictor in gradient boosting corrects the error of its predecessor and is trained using the residual errors of the predecessor labels. Further XG- Boost and CAT Boost algorithm were included in this study with early stopping parameters to prevent over fitting.

### D. XG BOOST
XG Boost is a gradient-boosted decision tree implementation. In this approach, consecutive decision trees are generated in which weights play a crucial role. All independent variables are allocated weights, which are subsequently input into the decision tree used to predict outcomes. The weight of variables for which the tree made incorrect predictions are raised and these variables are then given to a second decision tree. The ensemble of these independent classifiers/predictors yields a robust and more accurate model. It can solve issues including regression, classification, ranking, and user-defined prediction.

Here, XG Boost is used in the regression model and let $\bar{y}_i$ be the predicted value of the model given by:-

$$\bar{y}_i = \sum_{k=1}^{K} f_k(x_i) \quad (24)$$

where $f_k$ represent the independent regression tree and $f_k(x_i)$ denote the prediction score given by k-th tree to i-th sample. In the regression tree model, the collection of functions $f_k$ may be learnt by minimising the objective function: -

$$obj = \sum_{i=1}^{n} l(y_i, \hat{y}_i) + \sum_{k=1}^{K} \mu(f_k) \quad (25)$$

The $l$ here is a training loss function that measures the difference between the predicted $\hat{y}_i$ and the train object $y_i$. The term $\mu$(*learning rate*) penalises the complexity of
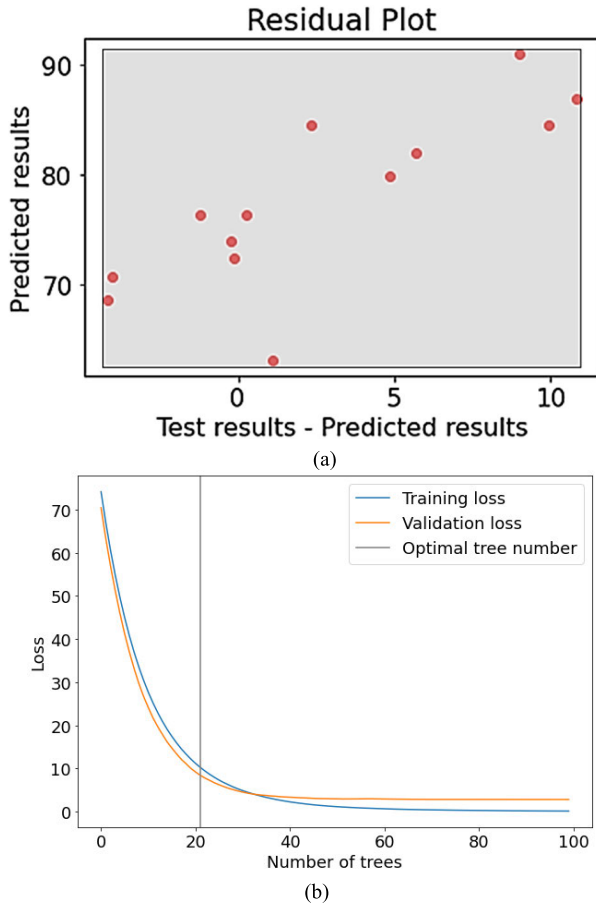
**FIGURE 13.** (a) Residuals plot for XG Boost with RMSE = 5.51 and $R^2$ =0.792 (b) Plot for training and validation loss with early stopping of 20.



**FIGURE 14.** (a) Residuals plot for CAT Boost with RMSE =2.5 and $R^2$ = 0.95 (b) plot for training and validation loss with early stopping of 20.

the projected model to prevent overfitting and is given by [17]:-

$$\mu\left(f_k\right) = \gamma T + \frac{1}{2}\lambda\|\varphi\|^2 \qquad (26)$$

where $\gamma$ and $\lambda$ are the degrees of regularization T and $\varphi$ are the number of leaves and the scores on each leaf in a decision tree respectively. Further, additional ensembles of trees may be taught in an additive fashion. The training and test datasets were divided in the ratio of 80:20 as it provides minimum root mean square error (RMSE) and maximized $R^2$ value as compared to other training and test sets combination. Since, the XG Boost suffers from overfitting, therefore, early stopping parameter is utilized with optimal epoch of 20. As seen in Figure 13, the residuals (ablation percentage) vary between -4 and 11, with the majority of residuals being within the permissible range. The learning rate ($\mu = 0.1$) was set low to prevent the data from being overfitted. This, however, leads to a deviation from the projected values. Further, as seen in Figure 12(b), the optimal number of decision trees in XG Boost to predict the desired result was considered to be 20. However, the loss function reaches the minimum value at 40 which results in an increase in computation time of the boosting algorithm. Also, although the predicted outcome is
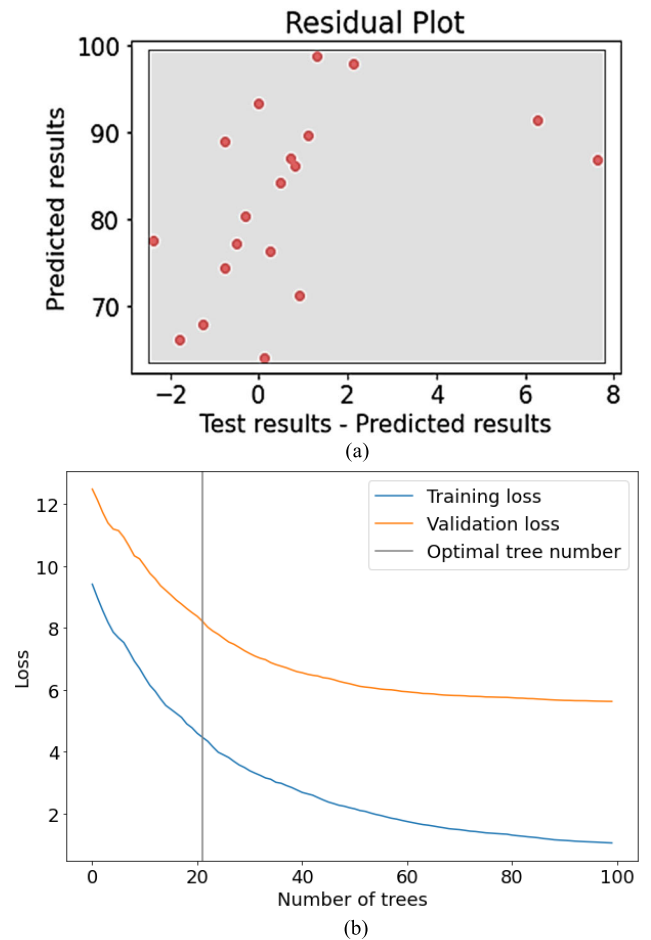
satisfactory with RMSE of 5.51 and $R^2$ of 0.79 but other gradient boosting algorithm is exploited to further improve the results. In such a case CAT Boost is preferred as Light GBM algorithm have similar accuracy score as compared to XG Boost [18].

## V. CAT BOOST

Cat Boost is an open-source implementation of Gradient Boosted Decision Tree (GBDT) for Supervised Machine Learning that features two innovations: Ordered target statistics and ordered boosting.

In Cat Boost, random permutations of training dataset are generated which uses many permutations to increase the robustness of the algorithm and then selects a random permutation to derive gradients from it. These are the same permutations used for generating categorical feature statistics. For each permutation $\sigma$, $n$ different models are trained. That means that for building one tree $O\left(n^2\right)$ need to be stored and recalculated for each permutation $\sigma$ and for each model $M_i$, $M_i\left(X_1\right),\ldots, M_i\left(X_i\right)$ model need to be updated. Thus, the resulting complexity of this operation is $O\left(sn^2\right)$. Using a crucial technique, the complexity of tree building is lowered in practical implementation to O(sn), for each permutation,
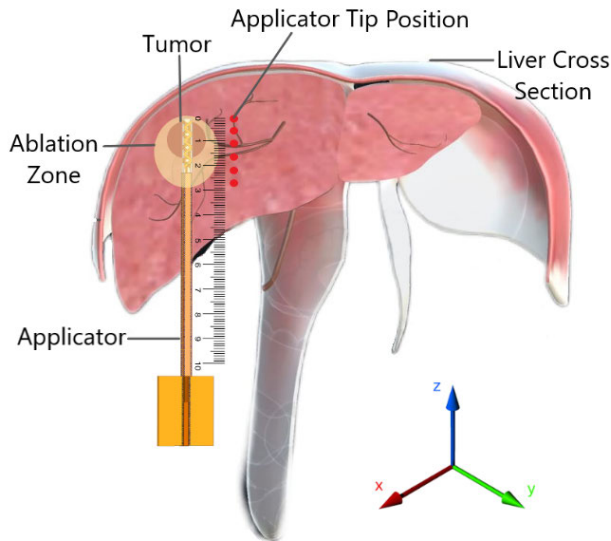
**FIGURE 15.** Model depicting positioning of applicator in HCC and acquiring datasets for ML algorithm.

**TABLE 5.** Performance analysis of different ML algorithm used in this work.

| ML Algorithm | Training set : Test set | R$^2$ value | RMSE |
|---|---|---|---|
| Linear Regression | 80:20 | 0.46 | 7.35 |
| Polynomial Regression | 80:20 | 0.95 | 2.31 |
| SVR-Sigmoid | 80:20 | -0.01 | 10.17 |
| SVR-Poly | 80:20 | 0.80 | 4.46 |
| SVR- Rbf | 80:20 | 0.91 | 2.94 |
| CAT Boost | 70:30 | 0.95 | 2.50 |
| XG Boost | 80:20 | 0.792 | 5.51 |

instead of storing and updating $O(n^2)$ values $M_i(X_j)$, $M'_i(X_j)$, $i = 1, \ldots, [log_2(n)]$, $j < 2^{i+1}$ values are maintained, where $M'_i(X_j)$ is the approximation for the sample $j$ based on the first $2^i$ samples. Thus, the number of predictions $M'_i(X_j)$ is not larger than $\sum_{0<i<log_2(n)} 2^{i+1} < 4n$. On the basis of the approximation, the gradient of the example $X_k$ used to choose a tree structure is calculated based on the approximation $M'_i(X_k)$, where $i = [log_2(k)]$ [18].

The training and test datasets were divided in the ratio of 70:30 as it provides minimum root mean square error (RMSE = 2.50) and maximized R$^2$ (0.95) value as compared to other training and test sets combination.

As shown in the Figure 14, the CAT Boost algorithm performs better than the other gradient boosting algorithms with predicted ablation percentage has error margin of −2 to 7 percent due to ordered boosting.

In addition, as explained above, since fewer trees are needed to predict the ideal value, the loss factor decreases more rapidly for 20 optimal trees than for the XG boost method. Since loss optimization and residues are smaller than XG boost, this technique may be employed more effectively when determining the ideal antenna site for maximum ablation.

Since this is a simulation-based study and complex biochemical process is not taken into account, therefore, a similar dataset can be attained from an ex-vivo setup as well for further calibration, if required. As shown in the figure 15, a cross-sectional incision is made in bovine liver and the antenna applicator is placed in the tumor along with the measurement scale. Further, the tip position is changed along z-axis and the percentage of the ablation zone is calculated as per the equation 15. The procedure is repeated for different tumor sizes. However, this is one-time process and do not require data acquisition before every clinical procedure. Also, the ablation zone generated by the antenna is up to 36 mm

therefore, the optimal localization should not exceed the maximum ablation capability of the applicator.

## VI. RESULTS AND DISCUSSION

The proposed antenna structure shows good impedance matching due to SICL and impedance transformation structure. The $S_{11}$ obtained for 30 mm tumor diameter is −24 dB as shown in the Figure 2. Further due to the insertion of a transition layer between the SICL and impedance transformation structure and tapping the antenna at optimal location predominately reduced the surface current along the antenna axial direction and hence the elongated ablation zone, as contrary in recent articles, is minimized as shown in the Figure 4.

In this paper, a coupled electromagnetic field and heat transport model is solved using a 3D finite element approach (FEM). The simulated environment consists of temperature dependent permittivity and conductivity. For 10 minutes of ablation time 32 mm transversal diameter of tumor is observed which spherical ablation zone as shown in the Figure 6. Further, since the permittivity of tumor depends upon the level of malignancy, Figure 7 shows the specific absorption rate for permittivities ranging from 25,35 and 55, and can be concluded that the increase in permittivity reduces the SAR and can severely impact the ablation zone of the antenna. Additionally, Figure 8 proves the sphericity of the ablation zone.

Since the optimal localization of the antenna applicator is of utmost importance for achieving the maximum ablation zone and also significantly reduces the chances of ablating healthy tissue, machine learning algorithms are considered. All the python code used in ML algorithm is performed in Google Colaboratory.

Further, at first the basic linear regression is used to predict the ablation percentage from the tumor location but the deviations observed were large as compared to the target output as shown in the Figure 9. Further, since polynomial regression involves better curve fitting, the results obtained were close to the target value but are not optimal since 4$^{th}$

**TABLE 6.** Comparative analysis of newly released works.

| Published Work | Input Power (W) | Operating Frequency (in GHz) | Antenna Probe area (in mm²) | Ablation zone (mm) | Application time (min.) | Volume Of ablation zone (cm³) | Aspect Ratio |
|---|---|---|---|---|---|---|---|
| Hung et al. [19]* | 42 | 10 | 9.61 | 20 (T) 44 (A) | 5 | 9.21 | 0.45 |
| Hung Luyen et al. [7]  * | 42 | 1.9 | 8.03 | 40 (T) 50 (A) | 10 | 41.86 | 0.8 |
| Hessinger C et al [6] | 20 | 5.8 | 3.79 (without catheter) | 22 (T) 28 (A) | 10 | 7.1 | 0.78 |
| Moon Lee et. al. [20] | 50 | 2.45 | 7.06 | 30-40 (T) | NA | NA | NA |
| Eman G. et al. [21]* | 3 | 7.3 | 11.93 | 16 (T) | 3 | NA | NA |
| Amira S. Ashour [22]* | 20 | 2.45 | 11.93-12.56 | 28.42 (T) | 10 | NA | NA |
| Burak Uzman [23]* | 50 | 2.45 | 7 | 33.6 (A) | 5 | NA | NA |
| Singh,Yadav* [24] | 20 | 5 | 8.03 | 32 (T) 44 (A) | 5 | 23.579 | 0.72 |
| Li Wang [25] | 20 | 2.45 | 4.46 | 20(T) 35(A) | - | 7.326 | 0.57 |
| This work* | 20 | 2.45 | 3 mm width 1.25 mm height (with Catheter | 32 (T) 25 (A) | 10 | 13.061 | 0.78 |

*The highlighted article contains the simulated value.*

order polynomial is required to predict the result which is complex. Further support vector regression (SVR) is used to predict desired output. Since, the output of SVR is dependent on loss function and type of kernel used in the hyperplane, three types of kernels were used namely ploy, rbf, and sigmoidal and shown in the Figure 11. The rbf and poly kernel performed well with high $R^2$ value and low RMSE, as shown in Table 5. However, a high regularization constant $C$ was selected in order to fit the data which may result in overfitting of the dataset. Therefore, gradient boosting algorithm was incorporated and the overfitting is prevented by utilizing early stopping parameters.

The efficient prediction outcome of ML algorithms depends on roundness of ablation zone since elongated ablation pattern may complicate the ablation zone prediction and also destroys the healthy tissue. Therefore, aspect ratio (ratio of minimum ablation diameter to maximum ablation diameter) is an important parameter for efficient use of applicator as shown in table 6.

Table 6 compares various recently published articles with the proposed work. Different crucial parameters reported were included in the comparison, such as power setting, frequency of operation, antenna dimension, application time, and volume of the ablation zone. An antenna with low input power may facilitate better power handling capacity. Additionally, as input power is increased, the water content boils off, resulting in an impedance mismatch and heating of the applicator, resulting in a more elongated pattern in the axial (A) direction [6], [19]. Additionally, since blood in arteries functions as a heat sink owing to its thermos-regulation nature, a more rapid ablation is necessary. However, Hassan et al. [21] used a lower input power but a higher operating frequency resulting in a more rapid dielectric rotation of the polar molecules and thus, a faster dielectric heating. However, since applied input power has a more significant impact on the ablation zone, therefore, lower power setting may be used for smaller tumors. Since only a few articles provide the overall ablation volume, therefore, to have an analogous comparison, the equation reported used to calculate the ablation volume is as followed in [6]. The proposed work provided a better transversal ablation zone at similar power input.

$$Ablation\ Volume = \frac{4\pi}{3} \left(\frac{T}{2}\right)^2 \left(\frac{A}{2}\right) \quad (27)$$

Also, to reduce complexity and overfitting arising from the $4^{th}$-order polynomial as in polynomial regression and SVR-poly, XG Boost and CAT Boost algorithm were incorporated. Since the CAT Boost algorithm requires lesser number of decision trees to converge to the optimal results and also provide optimal $R^2$ and RMSE value as shown in Table 5, it can be a better algorithm for prediction of percentage of ablation.

This study shows that the roundness of ablation zone is an important parameter in prediction of ablation percentage efficiently. The novel applicator not only achieve near spherical ablation zone but also provide considerable ablation zone within application time. Further, the estimated ideal probe location acquired by the ML algorithm for the proposed antenna provides the percentage of ablation for specific locations and since most of the MWA requires image guided mechanism to insert the applicator into the tumor, therefore, strategically placing the applicator as per the tumor size and antenna tip location from the center of the tumor, the machine learning algorithm such as CAT boost would be able to predict the ablation percentage beforehand. Such a technique not only predicts whether a tumor will be ablated completely or not (beforehand) but also is helpful in better optimization of power delivery by restricting over/under ablation. Over-ablation may lead to the destruction of healthy tissue nearby and under-ablation may lead to the recurrence of Tumor

However, such a study is FEM based and further in-vitro analysis is required as few assumption is incorporated in this model such as no protein denaturation or other complex biochemical process are considered, also, the liver tissue and embedded tumor do not undergo any deformation during heating.

## VII. CONCLUSION

This study presents a novel SIW based antenna working at 2.45 GHz. The cross-like antenna element which resembles a normal mode helix is used to ablate the tissue mainly in the broadside direction.

The use of SICL and impedance transformation structure provides impedance matching at 50 ohm which successfully suppresses the surface current and hence reduced the elongated ablation zone along the axial direction and therefore localize the ablation zone to tumor tissue only. Such a roundness in ablation zone not only prevent over ablation but also help in prediction of the ablation percentage with changing position of the applicator and hence can be advantageous in maximum ablation of the tissue with optimum use of power.

The temperature-dependent conductivity and permittivity study is introduced in this study as such tissue properties change with the change in temperature.

In this regard, a 3-D model of human liver tissue containing the tumor is simulated using the FEM software. The antenna probe is then inserted into the tumor. The proposed antenna successfully ablated the tumor with diameter up to 32 mm in transversal direction and 25 mm along the axial direction.

Further, since optimal localization of the antenna is of utmost importance to destroy the tumor, various machine learning algorithms were exploited. The polynomial regression with $4^{th}$ order provided satisfactorily prediction but suffers from over-fitting of the data while SVR with rbf kernel also yield good prediction of the ablation percentage but also tends to overfit with higher regularization parameter $C$. Further, to eliminate overfitting gradient boost algorithms were incorporated and the results obtained by CAT Boost algorithm among various ML algorithm is found to be optimum for actual clinical outcomes with high $R^2$ value and low RMSE.

## REFERENCES

[1] K. A. McGlynn, J. L. Petrick, and H. B. El-Serag, "Epidemiology of hepatocellular carcinoma," *Hepatology*, vol. 73, no. 1, pp. 4–13, 2021.

[2] B. Radjenovic, M. Sabo, L. Soltes, M. Prnova, P. Cicak, and M. Radmilovic-Radjenovic, "On efficacy of microwave ablation in the thermal treatment of a hepatocellular carcinoma," *Cancers*, vol. 13, no. 22, p. 5784, 2021.

[3] C. L. Brace and S. Etoz, "An analysis of open-ended coaxial probe sensitivity to heterogeneous media," *Sensors*, vol. 20, no. 18, p. 5372, 2020.

[4] K. Imajo, Y. Ogawa, M. Yoneda, S. Saito, and A. Nakajima, "A review of conventional and newer generation microwave ablation systems for hepatocellular carcinoma," *J. Med. Ultrason.*, vol. 47, no. 2, pp. 265–277, Apr. 2020.

[5] M. B. Glassberg, S. Ghosh, J. W. Clymer, R. A. Qadeer, N. C. Ferko, B. Sadeghirad, G. W. Wright, and J. F. Amaral, "Microwave ablation compared with radiofrequency ablation for treatment of hepatocellular carcinoma and liver metastases: A systematic review and meta-analysis," *OncoTargets Therapy*, vol. 12, pp. 6407–6438, Jan. 2019.

[6] C. Hessinger, B. Bazrafshan, M. Schußler, S. Schmidt, C. Schuster, F. Hubner, T. J. Vogl, and R. Jakoby, "A dual-mode coaxial slot applicator for microwave ablation treatment," *IEEE Trans. Microw. Theory Techn.*, vol. 67, no. 3, pp. 1255–1264, Mar. 2019.

[7] H. Luyen, S. C. Hagness, and N. Behdad, "A balun-free helical antenna for minimally invasive microwave ablation," *IEEE Trans. Antennas Propag.*, vol. 63, no. 3, pp. 959–965, Mar. 2015.

[8] Z. Wen, X. Lin, C. Li, Y. Yan, and D. Liu, "A helical dipole antenna for microwave ablation based on substrate integrated coaxial line technology," in *Proc. IEEE Asia–Pacific Microw. Conf.*, Dec. 2021, pp. 804–806.

[9] J. A. Alzubi, O. A. Alzubi, M. Beseiso, A. K. Budati, and K. Shankar, "Optimal multiple key-based homomorphic encryption with deep neural networks to secure medical data transmission and diagnosis," *Exp. Syst.*, vol. 39, no. 4, May 2022, Art. no. e12879.

[10] M. Tao, Y. Wu, Z. Jiang, and Z. Hao, "Ultra-wideband low-loss transition for the SIW to the SICL," *IET Microw., Antennas Propag.*, vol. 13, no. 11, pp. 1764–1767, Sep. 2019.

[11] J. Hristov, "Bio-heat models revisited: Concepts, derivations, nondimensalization and fractionalization approaches," *Frontiers Phys.*, vol. 7, Nov. 2019, p. 189.

[12] A. Bottiglieri, G. Ruvio, M. O'halloran, and L. Farina, "Exploiting tissue dielectric properties to shape microwave thermal ablation zones," *Sensors*, vol. 20, no. 14, pp. 1–15, 2020.

[13] Z. Ji and C. L. Brace, "Expanded modeling of temperature-dependent dielectric properties for microwave thermal ablation," *Phys. Med. Biol.*, vol. 56, no. 16, pp. 5249–5264, Aug. 2011.

[14] S. Nandi, B. Ballotta, S. Rampino, and V. Barone, "A general user-friendly tool for kinetic calculations of multi-step reactions within the virtual multifrequency spectrometer project," *Appl. Sci.*, vol. 10, no. 5, p. 1872, Mar. 2020.

[15] S. Ghosh, A. Dasgupta, and A. Swetapadma, "A study on support vector machine based linear and non-linear pattern classification," in *Proc. Int. Conf. Intell. Sustain. Syst. (ICISS)*, Feb. 2019, pp. 24–28.

[16] D. Basak, S. Pal, D. Ch, and R. Patranabis, "Support vector regression," *Neural Inf. Process.-Lett. Rev.*, vol. 11, no. 10, pp. 203–224, Oct. 2007.

[17] T. Chen and C. Guestrin, "XGBoost: A scalable tree boosting system," in *Proc. 22nd ACM SIGKDD Int. Conf. Knowl. Discovery Data Mining*. New York, NY, USA: Association for Computing Machinery, 2016, pp. 785–794.

[18] J. T. Hancock and T. M. Khoshgoftaar, "CatBoost for big data: An interdisciplinary review," *J. Big Data*, vol. 7, no. 1, pp. 1–45, Dec. 2020.

[19] H. Luyen, F. Gao, S. C. Hagness, and N. Behdad, "Microwave ablation at 10.0 GHz achieves comparable ablation zones to 1.9 GHz in ex vivo bovine liver," *IEEE Trans. Biomed. Eng.*, vol. 61, no. 6, pp. 1702–1710, Jun. 2014.

[20] M. Lee and T. Son, "Helical slot antenna for the microwave ablation," *Int. J. Antennas Propag.*, vol. 2019, pp. 1–9, Oct. 2019.

[21] E. G. M. I. Hassan, H. Takruri, and A. I. Zaki, "Realization and experimental assessment of baseball-bat microwave antenna for low power cancer ablation," *IEEE J. Electromagn., RF Microw. Med. Biol.*, vol. 4, no. 2, pp. 133–139, Jun. 2020.

[22] A. S. Ashour, M. Asran, W. S. Mohamed, and D. I. Fotiadis, "Optimal localization of a novel shifted 1T-ring based microwave ablation probe in hepatocellular carcinoma," *IEEE Trans. Biomed. Eng.*, vol. 68, no. 2, pp. 505–514, Feb. 2021.

[23] B. Uzman, A. Yilmaz, H. Acikgoz, and R. Mittra, "Graphene-based microwave coaxial antenna for microwave ablation: Thermal analysis," *Int. J. Microw. Wireless Technol.*, vol. 13, no. 5, pp. 497–505, Jun. 2021.

[24] S. K. Singh and A. N. Yadav, "Design of a novel externally-tapped intertwining helical antenna for microwave ablation and its statistical analysis on tissue model," *Int. J. RF Microw. Comput.-Aided Eng.*, vol. 31, no. 12, pp. 1–16, Dec. 2021.

[25] L. Wang, X. Bao, Y. Wang, G. Crupi, and A. Zhang, "A localized and minimally invasive tumor treatment based on a frequency adjustable microwave ablation method," in *Proc. IEEE Int. Symp. Med. Meas. Appl. (MeMeA)*, Jun. 2022, pp. 1–6, doi: 10.1109/MeMeA54994.2022.9856429.

**SUYASH KUMAR SINGH** received the B.Tech. degree in electronics and communication engineering from the Jaypee University of Engineering and Technology, India, and the M.E. degree in wireless communication from the Birla Institute of Technology, Ranchi, India. He is currently pursuing the Ph.D. degree with the Indian Institute of Information Technology, Allahabad, India. He has published several international journals. His research interests include microwave ablation antennas, passive and active microwave components, the use of machine learning, and artificial intelligence in microwave circuits/antennas.

**AMAR NATH YADAV** was born in 1986. He received the Ph.D. degree from IIT Guwahati, in 2019, and the M.Tech. degree from IIT Roorkee. He is currently an Assistant Professor with the Indian Institute of Information Technology, Allahabad. He has published several international journal articles and conference papers. His research interests include microwave circuits and antennas.

• • •